[1] Ashwin Narasimha Murthy
[2] Ramesh Krishnamaneni
[3] T. Prabhakara Rao
[4] V. Vidyasagar
[5] Dr. Ambhika. C
[6] I. Naga Padmaja
[7] Manasa Bandlamudi
[8] Dr. Amit Gangopadhyay

Deep Long and Short Term Memory with Tunicate Swarm Algorithm for Skin Disease Detection and Classification

Abstract: - The development and implementation of cost-effective and efficient screening technologies is important. To address these concerns, we have introduced a unique method to detect skin diseases. Each photo is first pre-processed and cropped to pixel size. Six square fields are used to split these pictures into pixels. Techniques for enlarging images, such as rotation, mirroring, and enhancement, are employed to minimize the quantity of parameters needed for further processes. An kernel-weighted fuzzy local information or the C-means clustering model (K-FCM) is used to properly segment cancer-affected regions. Texture and colour features are then extracted. Finally, a deep long-term and short-term memory (DLTM)-based tunicate group algorithm (TSA) is used to detect skin diseases and classify both normal and abnormal classes. The experiment was carried out using MATLAB, and photos were gathered from the Helllev University Hospital in Denmark. According to the comparative analysis results, the proposed DLSTM-TSA outperforms competing products in terms of F-score, sensitivity, and precision.

Keywords: Skin disease, Tunicate swarm algorithm, Deep LSTM, Herlev University Hospital and Performance metrics.

1 INTRODUCTION:

The pores and skin is the principle appendage of the human body, which consists of subcutaneous, dermis, and epidermal tissues, in addition to muscle mass, nerves, lymphatic veins, and blood vessels, that could protect the frame and sense external temperature [1-4]. [1-4]. The pores and skin, which covers the entire body, can guard many tissues and organs from external impacts along with the immune machine, infectious viruses, chemical damage, and synthetic pores and skin damage. It additionally prevents the lack of lipids and water inside the dermis and epidermis, preserving the pores and skin's barrier characteristic. Because the pores and skin is the body's largest organ, the outcomes of inflammatory, bacterial, and viral diseases tour throughout the frame, causing a extensive variety of health issues [5]. Vitiligo,wrinkles, atopic dermatitis, psoriasis, wounds, photo growing older, melanoma, morphea, alopecia, zits, and different skin issues are among them. lots of those diseases can be healed if they're caught early sufficient before they spread [36]. Dermoscopy is a way that uses polarized light to lessen surface reflections. it's miles used by specialists to look at adjustments within the skin using intense mild. in spite of its protecting and barrier features.

The skin is constantly exposed to various external and genetic variables, so it is not indestructible. Currently, the human body is affected by three categories of skin diseases: allergic skin diseases, fungal skin diseases, and viral skin diseases [6-8].Although many skin diseases are currently treatable, they place a significant burden on patients' lives. Currently, most knowledge about a patient's existing symptoms is usually based on the physician's years of

[1] Software development manager, Amazon, 440 Terry Ave N, Seattle, WA 98109, United States. Email: ashmurthy10@gmail.com
[2] Solutions Architect, IBM, 1 Alhambra Plaza Columbus Ctr, Suite 1415Coral Gables, FL 33134-5216, US. Email: Rameshkr@us.ibm.com.
[3]Associate Professor, Department of Computer Science and Engineering, Aditya University, Surampalem, Andhra Pradesh,533437.
[4] School of Technology Management and Engineering, SVKM's Narsee Monjee Institute of Management Studies Deemed-to-be University, Hyderabad Campus, Mahbubnagar, Telangana 509301, India. Email: vidyasagar.voorugonda@nmims.edu.
[5]Associate Professor, Department of Artificial Intelligence and Machine Learning, R.M.D Engineering College, R.S.M Nagar, Kavaraipettai, Gummidipoondi Taluk, Tiruvallur District, Tamil Nadu, India, Pin code: 601 206. Email: ambhidurai@gmail.com.
[6] Assistant Professor, Department of Information Technology, R.V.R&J.C College of Engineering, Guntur. Email: nagapadmaja.indeti@gmail.com.
[7]Assistant Professor, Department of Information Technology, R.V.R&J.C College of Engineering, Guntur. Email: manasabandlamudi@gmail.com.
[8]Professor, Department of Electronics and Communication Engineering, Mohan Babu University (Erstwhile Sree Vidyanikethan Engineering College), Tirupati-517102, Andhra Pradesh, India. Email: ag102091@gmail.com

experience or his or her own subjective assessment, which can lead to errors and, as a result, delays in treatment there is.

It's possible that the skin lesions are either primary or secondary [9]. Bulla, cyst, pustule, vesicle, tumour, nodule, discolouration, spots, pimples and plaque becomes main skin lesions, when atrophy, maceration, umbilication, phyla, ulcer, fissure, indurations, excoriation, and erosion are secondary skin lesions. Distribution , configuration are two words that are connected to skin lesions [37]. The pattern denotes the lesions grouping, while the sharing denotes the location of lesions. Based on the basic three types of skin infections are mostly studied in literature, more skin connected image segmentation and classification are covered in this work. Likewise, supervised methods grouping such as SVM are widely used, but they have a number of essential parameters that must be identified and set correctly in order to achieve better results and more precise classifications. To overcome the challenges of existing research, we proposed to introduce a capsular group formation algorithm based on deep long-term and short-term memory for image recognition of skin diseases. This document's remaining sections are arranged as follows. Related work is discussed in Section 2, and the suggested technique is covered in Section 3 after that. In Section 4, the experimental results are discussed. Section 5 brings the process to a close.

2.Related works:

Bhadula et al. [10] propose machine learning (ML) methods to categorize the skin disease images. To predict the exact kind of skin disease, the five different machine learning algorithms were chosen and used to a data collection of skin infections. We've worked with CNN, kernel SVM, logistic regression, nave bayes, and Random forest, among a few machine learning methods. A comparable investigation based on training accuracy and confusion matrix parameters has been carried out and graphed. CNN has been discovered to have the highest training precision for the correct prediction of skin disorders of all the candidates and this method is not applicable for real time data.

A mix of crossover brain networks was created by Chakra borty et al. said. [11]Image based diagnosis of skin sicknesses. Altered information from different method can be utilized to train hybrid fake brain networks approved with cloud heuristics to arrange skin pictures and analyze the illness in study. The ANN was prepared utilizing the Non-Prevailing Arranging Hereditary Calculation II, a multivariate improvement technique (NN-NSGA-II).Furthermore, with respect to the testing of topological disarray framework based execution measurements such as F-measure, recall, precision, and precision, others have proposed two met heuristics-based classifiers, namely ANN-trained with PSO (NN-PSO) and ANN (NN-CS) trained on Cuckoo Search. Experimental results show that the proposed NN-NSGA-II model with rich features is superior. Machine Learning and Image Processing (ML-IP) was developed by ALEnezi et al. he suggested. [12] Detects skin diseases. This is a method of digitally photographing the affected area of the skin and using image processing to identify the type of disease. This method is easy and quick and requires no expensive equipment other than a camera and computer. This method applies to colour image sources. The newly trained convolutional neural network is then used to resize the image and extract features. This function was then classified using multiclass SVM. Finally, the user is shown the results such as infection type, severity, and disease. This technology accurately detects three different skin diseases with a 100% cure rate.

Balaji et al. [13] introduced the use of a dynamic graph cut method with a Naive Bayes (GC-NB) classifier for skin disease segmentation and classification. The researchers wanted to use a new dynamic graph cut technique for skin lesion segmentation, followed by a Nave Bayes classifier to categorise skin illnesses. They tested our proposed method using the ISIC 2017 dataset and discovered that the outputs outperformed various comparative techniques, such as SegNet andFCN, by 6.5 percent and 8.7 percent. The International Skin Imaging Collaboration (ISIC) dataset is open for public study and experimentation on the website. On this data set, obtain 94.3 percent accuracy for benign cases, 92.9 percent for keratosisand91.2 percent for melanoma.

Khamparia et al. [14] introduced a deep learning (DL) framework for skin cancer classification. Fully automated features have been extracted from images utilising distinct pretrained configurations such as SqueezeNet, ResNet50, Inception V3 and VGG19, and fed into a fully connected layer of CNN. Completely integrate with an IoHT architecture and capable of assisting specialist doctors in the management and therapy of skin cancer from a distance. The suggested system beat existing pretrained designs in terms of accuracy, recall, and precision in detecting and classifying skin cancer from skin lesion images, according to performance metric evaluation.

3 Proposed Model:

As shown in Figure The general structure of the proposed work is shown in Figure 1. Preprocessing, segmentati on, feature extraction and skin classification are the stages of the plan. Finally the model's accuracy, specificity, sensitivity, AUC, and F-score are evaluated. The subsections below provide a more detailed explanation of each stage.

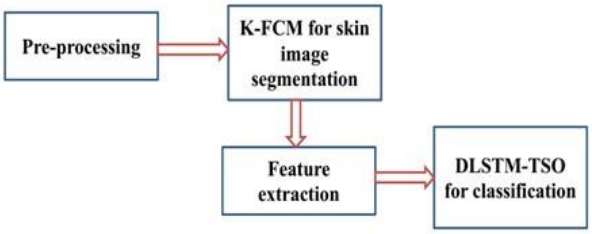

Figure 1: Proposed architecture

3.1Pre-processing:

Various normal and abnormal images in JPG format were acquired from three different classes. All JPG images have a primary matrix size of pixels. For each image, we first run a pre-processing step [15]. The images are first cropped into pixels, and then each one is divided into pixels using six square patches. Resize every original image into after that. The original images of 2112 are finally received.

3.3 Skin image segmentation based on Kernel weighted fuzzy local information c-means clustering (K-FCM):

While thinking that neighbourhood information affects current pixels, the FLICM method never has a regularisation parameter for fuzzy local information factor [16]. To improve the FLICM robustness to outliers and noises, Memo net al. [17] suggested the KFCM model by developing Kernel metrics and weighted trade-off fuzzy coefficients. The KFCM model is utilized to segment cervical cancer images in this investigation.

$$J_{KFCM}(A,B)=\sum_{l=1}^{N}\sum_{k=1}^{D}b_{lk}^{n}\left(\left\|\phi(z_l)-\phi(c_k)\right\|^2+G_{lk}\right) \tag{1}$$

The number of samples and clusters are defined as N and D respectively. The membership function z_l of the l^{th} cluster is b_{lk} in which a nonlinear map is denoted by ϕ. The membership of groups L is a nonlinear map represented by Eq. (2)

$$J_{KFCM}(A,B)=\sum_{l=1}^{N}\sum_{k=1}^{D}b_{lk}^{n}\left[(1-K(y_l,a_k))+G_{lk}\right] \tag{2}$$

From this, fuzzy local feature is G_{lk} These include pixels' current ownership information, local area information, and grayscale information.

$$G_{lk}=\sum_{i\in N_{l,l\neq k}}\frac{1}{I_{l,k}}W_{lk}(1-a_{lk})^{n}(1-K(z_k,b_i)) \tag{3}$$

The degree membership of pixels close to the viewing window is defined as: The spatial Euclidean distance bet ween pixels, represented by the symbol. Local similarity emerged. Group center and degree members are shown below.

$$a_{il}=\frac{\left((1-K(z_l,b_k)+G_{il}\right)^{-1/n-1}}{\sum_{k=1}^{d}\left((1-K(z_l,b_k)+G_{il}\right)^{-1/n-1}} \tag{4}$$

$$a_i=\frac{\sum_{j=1}^{M}b_{i,l}^{n}K\left(z_l,a_i\right)z_l}{\sum_{j=1}^{M}b_{i,l}^{n}K\left(z_l,a_i\right)} \tag{5}$$

In FLICM, the squared Euclidean distance is replaced by a Gaussian kernel distance measure called KFCM [18] . Cancer regions of raw images were segmented using kernel-weighted fuzzy local C-means clustering (KFCM). 3.3 Feature extraction: The aim of this process is to extract the main features from the virus that lead to the ident ification and evaluation of the virus [19].

Colour Attribute: The average value of the colour of different colour channels is one of the most common colour attributes. Luminance, gray, hue and value (from the HSV colour space), red, green, blue (RGB), and chrominance were the colour channels used to capture colour differences (from the YCbCr colour space). In this article, we pick 10 features that represent the colour features of disease areas..

Texture Features:

Grayscale cooccurrence matrix (GLCM) is a grayscale image matrix. Texture analysis is based on the preferred method for selecting texture models. The texture of an image is characterized by counting the number of times a pixel of reference brightness appears on the skin in a spatial direction [20]. Identify regions using similarity, correlation, strength and variance of the GLCM matrix.

3.3 Skin disease detection and classification:

Deep Long and Short Term Memory with Tunicate Swarm Algorithm (DLSTM-TSA) are used for skin disease detection and classifications.

3.3.1 Deep Long and Short Term Memory (LSTM):

The prediction representation was urbanized using a conventional ANN that provides a direct mapping among the output prediction data and the input historical information [21]. The lack of time correlation in data series captures the link between time and data. Hidden neurons are defined by the following equation.

$$X_f^t = \sum_{j=1}^{I} W_f y_j^t + \sum_{f`=1}^{h} W_{f^{\sim}} Y_{f^{``}}^{t-1} \tag{6}$$

The input RNN with segment length y, hidden neurons (h), output neurons (O), and input neurons (I) are shown. The j^{th} input value y_j^t depends on y at time t. Network inputs to receptive neurons and latent neurons are latent neurons are X_j^t and Y_j^t . It is the value of the weight parameter W_f and the pass-back calculation method is explained by the formula below..

$$\delta_f^t = \sum_{k=1}^{O} \lambda_k^t W_{jf} + \sum_{f`=1}^{h} W_f \lambda_k^{t+1} \tag{7}$$

$$\delta_f^t = \frac{\partial \psi}{\partial X_i^t} \tag{8}$$

$$\frac{\partial \psi}{\partial X_{ij}} = \sum_{t=1}^{T} \frac{\partial \psi}{\partial X_i^t} \times \frac{\partial X_i^t}{\partial W_{ij}} = \sum_{t=1}^{T} \lambda_i^t Y_j^t \tag{9}$$

The capacity to utilize context oriented data while planning among information and result is a critical benefit of RNNs. The sensitivity of RNNs to input decreases in the early stages of training [22]. The performance of traditional RNN models is increased using LSTM. Back propagation over time (BPTT) model is used to update the weights of LSTM-based neurons from forward and backward training periods.

$$X_g^t = \sum_{t=1}^{I} W_{jg} y_j^t + \sum_{H=1}^{h} W_{Gf} B_g^{t-1} + \sum_{d=1}^{D} W_{Df} S_D^{t-1} \tag{10}$$

$$Y_g^t = f\left(X_g^t\right) \tag{11}$$

Forget gates has the following input and output values:

$$X_g^t = \sum_{t=1}^{I} W_{j\rho} y_g^t + \sum_{H=1}^{h} W_{f\rho} Y_f^{t-1} + \sum_{D=1}^{d} W_{D\rho} S_D^{t-1} \tag{12}$$

$$Y_\rho^t = f\left(X_\rho^t\right) \tag{13}$$

The input, state, and output are defined by the following equations:

$$X_D^t = \sum_{j=1}^{I} W_{jD} y_j^t + \sum_{f=1}^{h} W_{gD} Y_f^{t-1} \tag{14}$$

$$S_D^t = X_f^t H\left(X_D^t\right) + Y_\rho^t S_D^{t-1} \tag{15}$$

$$Y_D^t = Y_W^t F\left(S_D^t\right) \tag{16}$$

For output gates, the output and input values are as follows:

$$X_W^t = \sum_{j=1}^{I} W_{jW} y_j^t + \sum_{f=1}^{h} W_{gW} Y_f^{t-1} + \sum_{D=1}^{d} W_{DW} S_D^t \tag{17}$$

$$Y_D^t = f\left(X_W^t\right) \tag{18}$$

In the reverse step, we use the weights to update the LSTM neurons. The weight W_{ij} is from nodes j to nodes i. Memory, forgets, door and the entrance gatesare W_{DW} $W_{D\rho}$ W_{Dg} respectively. f is the gate function of each storage unit and the state storage unit is t. This is the storage function of the input/output storage. The total number of input values in the hidden layer is H. Moreover, the structure of the LSTM-RNN model is shown in Figure 2.

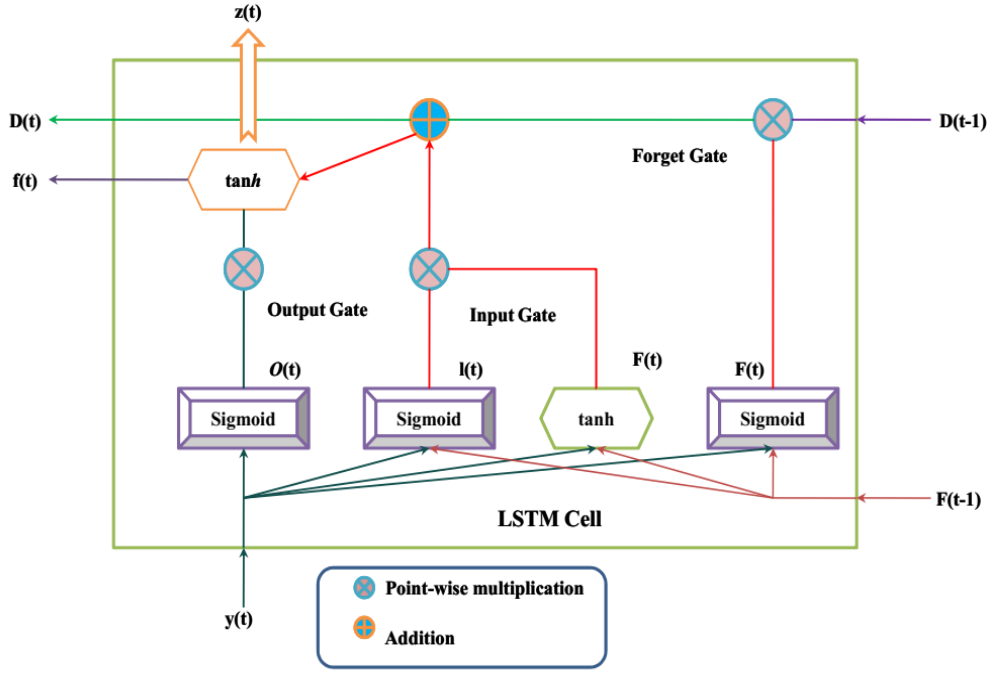

Figure 2: LSTM-RNN model construction

3.3.2 Tunicate Swarm Algorithm (TSA):

The tunicate is utilized for find out where seafood is located. Furthermore, tunicate features (Swarm intelligence combined with jet propulsion) identify the best food source [23]. In addition, the jet propulsion must meet three criteria: i) proximity to the search agent, ii) ignorance of agent divergence, and iii) progress toward the search agent. The best ideal solution will improve the properties of Swarm. In the next section, we'll look at the numerical expression.

i) Search Agents' Ignorance of Divergence:

By estimating a new position for the search agent, the divergence among the search agents can be denied.

$$\vec{E} = \frac{\vec{h}}{\vec{n}} \tag{19}$$

$$\vec{h} = x_2 + x_3 - \vec{G} \tag{20}$$

$$\vec{G} = 2.x_1 \tag{21}$$

$\vec{G}$ represents the water flow advection and $\vec{h}$ denotes the gravity force. 'x_1, x_2, and x_3' are the arbitrary variables and lies among 0 to 1 [24]. Additionally, the relationship strength of the searchers is also determined.

$$\vec{n} = [r_{\min} + x_1 . r_{\max} - r_{\min}] \tag{22}$$

Equation .17 establishes the initial and subordinate speeds are $r_{\min}$ and $r_{\max}$, as well as how they are used to generate social interaction. Let's have a look at the values of $r_{\min}$ and $r_{\max}$ is 1 and 4.

ii) ***The path to the best behaviour***

Search agents move to the best nearby location after ignoring neighbourhood disagreements.

$$\overrightarrow{IC} = \left| \overrightarrow{fs} - r_{andom} \cdot \overrightarrow{r_p(x)} \right| \tag{23}$$

The distance among the search agent and the food supply is represented here $\overrightarrow{IC}$. For the moment, *x* reflects the tunicate's current execution and determines the food source's location is $\overrightarrow{fs}$. The tunicate position $[Random \in 0,1]$ is denoted by an arbitrary constant $\overrightarrow{r_p(x)}$.

iii) Rate of convergence*:*

The rate of convergence amongst search agents is referred to as the convergence rate. The can's upgraded position $\overrightarrow{r_p(x)}$ is denoted by the symbol $\overrightarrow{fs}$.

$$\overrightarrow{r_p(x)} = \begin{cases} \overrightarrow{fs} + \vec{V} \cdot \overrightarrow{IC} & if \quad Random \geq 0.5 \\ \overrightarrow{fs} - \vec{V} \cdot \overrightarrow{IC} & if \quad Random < 0.5 \end{cases} \tag{24}$$

(i) The swarm's characteristics:

The placement of search agents is improved when the convergence rate is completed to duplicate the tunicate's swarm features.

$$\overrightarrow{r_p(x+1)} = \frac{\overrightarrow{r_p(x)} + \overrightarrow{r_p(x+1)}}{2 + b_1} \tag{25}$$

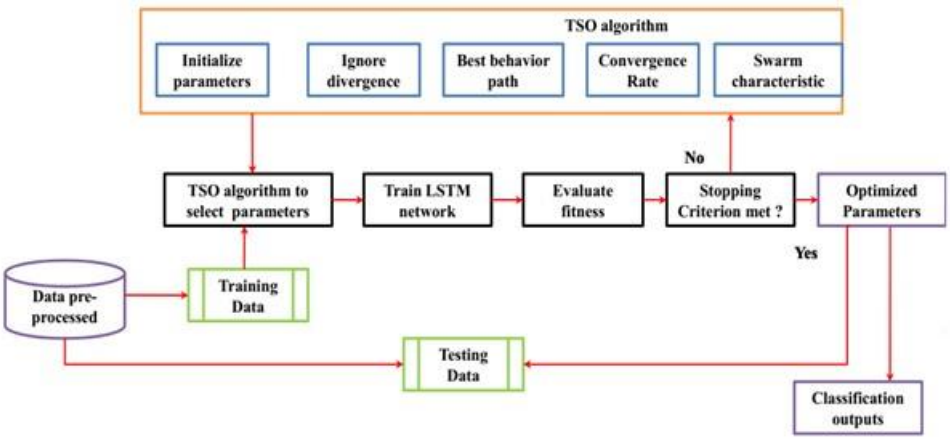

Figure 3: DLSTM based TSA algorithm for skin disease classification

3.4.3 LSTM with TSA for skin disease detection:

The ability to avoid missingness issues, reuse weight coefficients, and improve parameters when training a tradit ional RNN are advantages of DLSTM [25–
28].To solve these problems, Tunicate Swarm Algorithm (TSA) is used for parameter optimization of DLSTM i n skin disease detection. Because TSA takes less time, has good search ability, and provides other promising sea rch methods, including traditional optimization, ant colony algorithm, cuckoo search algorithm, chimpanzee opti mization algorithm and other algorithms. DLSTM-
based TSA selects the unit and time setting based on the classification of skin lesions according to the number of

LSTMs. To be successful, choosing the right time plays an important role. If the field of view is too large, the model will become a reference file. If the viewing area is too small, the model will remove important informatio n. The TSA block diagram of skin disease classification based on DLSTM is shown in Figure 3. In each primitiv e layer, TSA identifies the best hidden neurons and two hidden layers as follows, the real network cannot be buil t on DLSTM. In the DLSTM model, the input nodes and the hidden activation function are made using the hype rbolic tangent function.

Table 1: parameter settings for the DLSTM-TSA

Parameters	Ranges
Cover population	100
Maximum number of iterations	300
Learning rate	0.001
Modality	0.01
Number of units in completely associated layer l	30
Dropout	0.5
hidden state dimension	50
Batch size	50
Number of epochs	10
Power exponent	Directly diminishes from 0.1 to 0.3

An Exaggerated digression is an element of the scaled sigmoid capability. The output node's activation function is designed by the linear function [29]. The TSA is used to optimise the architectural parameters and the appropriate size of time windows in LSTM. Apply multiple numbers of LSTM units in each hidden layer and different time windows widths to validate the TSA fitness, which is based on the DLSTM, produces better categorization outputs like normal and abnormal cases of k in image.

4 Result and Discussion:

The MATLAB software performs experimental research for classification of skin disease. The advantage of the developed model is assessed using different of tests and state-of-the-art technologies [30-32]. Table 1 denoted the parameter settings for the DLSTM-TSA for skin disease analysis.

4.2 Dataset details:

As preliminary pictures, we checked out at skin illnesses from around the world. Dermnet furnished us with photographs. We considered skin disease pictures with regular. It has been determined that the accuracy of the preparation process varies depending on the type of skin disease. We've also gathered images from the internet. More than 500 images have been downloaded for ulcers, stasis dermatitis, lichen simplex chronics, eczema sub cute, eczema nummular, and eczema [33] and [34], which are five distinct illnesses.

4.3 Performance criterions:

The performance of DLSTM-TSA for identifying skin diseases has been validated using evaluation metrics such as accuracy, Matthews correlation coefficient (MCC), specificity, sensitivity, precision, and F-measure [35]. We use a standard performance measure called accuracy to examine the ratio of correct examples to all instances participating in the testing process (A). Accuracy is calculated using Equation (26)

$$. A = \frac{Tn + Tp}{Tn + Tp + Fn + Fp} \tag{26}$$

Specificity is the real negative proportion that is accurately characterized as negative as follows:

$$Specificity = \frac{Tn}{Fp + Tn} \tag{27}$$

Specificity or recall, the equation (28), is the proportion of actual positives that are correctly classified as positive.

$$Sensitivity = \frac{Tp}{Fn + Tp} \tag{28}$$

Precision (P) is defined as the proportion of abnormal predicted classes that is really correct.

$$P = \frac{Tp}{Fp + Tp} \tag{29}$$

The F-measure, which balances precision (P) and recall (R), is the harmonic mean it is a measure of test accuracy. The recall and F-score formula is calculated using equation (30) and (31).

$$R = \frac{Tp}{Fn + Tp} \tag{30}$$

$$F-score=2\left(\frac{R\times P}{P+R}\right) \tag{31}$$

Unbalanced datasets give overly optimistic and exaggerated results. Accuracy and Matthews correlation coefficient (MCC) are the most important metrics for evaluating dataset models. Classification performance is evaluated using three confusion matrix scores. The MCC interval range is -1 to 1. The skin infection expectation is addressed by a MCC worth of 1, the irregular forecast is addressed by a worth of 0, and the complete change is addressed by a worth of - 1. . The design of MM is shown likewise. (32)

$$MCC=\frac{(Tn+Tp)-(Fn\times Fp)}{\sqrt{(Tn+Fn)(Tn+Fp)(Tp+Fn)(Tp+Fp)}} \tag{32}$$

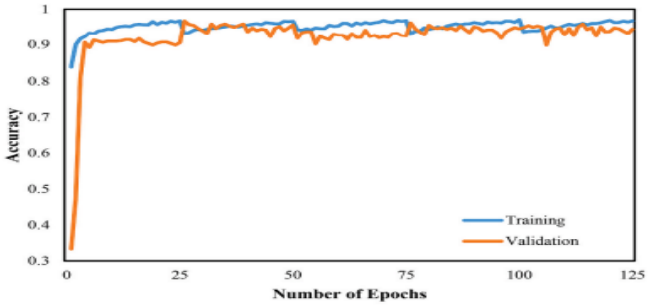

Figure 4: Performance analysis of accuracy

4.4 Performance Evaluation:

Figures 4 and 5 shows the performance analysis of skin disease classification in terms of accuracy and loss. Figure 4 graphically depicts the accuracy and power consumption based on a training and validation example results. The validation accuracy and training accuracy at each epoch were 97.0 percent and 98.3 percent, respectively (see Figure 4) reliability on both training and validation sets was above 96%. As shown in Figure 5, the validation and training losses were 0.07 % and 0.05 %.

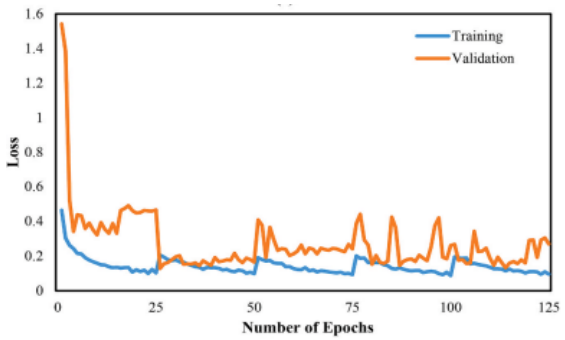

Figure 5: Performance analysis of loss

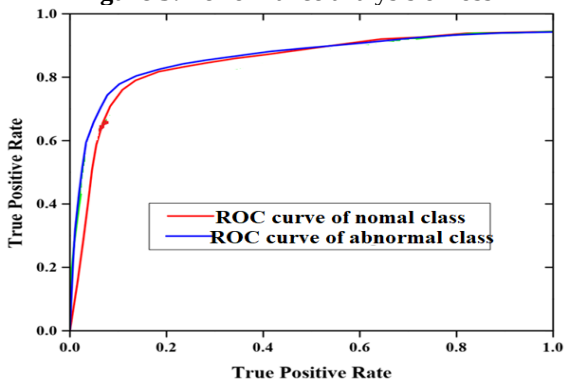

Figure 6: ROC curve performance analysis based on normal and abnormal classes

Figure 6 shows the performance of each group based on ROC data. Show the curve between false positives and true positives. The total number of correct predictions is divided by the number of false positives and true positives. The intrinsic value is called return or sensitivity. The class-based ROC curve plot shows the performance of the binary classification model.. The balance of predictions might change the classification threshold depending on the trade-off between false and true positive rates. The normal and a ROC curves vary in accuracy, reaching 0.88 percent, 0.92 percent, and 0.93 percent respectively.

The class- Table 2 shows the recommended DLSTM of TSA for classifying skin disease outcomes into classes. B. Normal, and Abnormal. For the regular class, we achieved 91 % precision, 92 % recall, 91 % F-measure, and 90% precision. Additionally, 95% precision, 94% precision, 92% recall, and 94% F-measure are achieved for the a normally class.

Table 2: The proposed LSTM-RNN based TSA for classification of skin disease results based on each class

Classes		Normal	Abnormal
Performance measures	Accuracy	92%	95%
	F-measure	91%	94%
	Recall	92%	92%
	Precision	91%	94%

We use K-FCM to evaluate improved segmentation results based on structural similarity index measurement (SSIM) and DICE parameters. The spatial relationship between the pixels of the test image (o) and the image used by the SSIM(s) is modified by different method

$$SSIM(I_o, I_s) = \frac{(2\delta_o\delta_s + V_1) + (2\sigma_{os} + V_2)}{(\delta_o^2 + \delta_s^2 + V_1)(\delta_o^2 + \delta_s^2 + V_2)} \tag{33}$$

As a result, the average and variances are δ and δ^2 respectively. Where the stabilising factor is V and the covariance of *s* and *o* is. DICE measurements are used to determine the similarity of two photos based on the number of pixels they share. DICE is used to quantify the spatial overlap between automatic segmentation and the ground truth. Figure 7 shows the proposed segmentation results for each class using SSIM and DICE measurements. When using the K-FCM algorithm, higher DICE and SSIM scores indicate better segmentation results.

$$D = \frac{2|Z \cap Q|}{|Z \cap Q| + |Z \cup Q|} \tag{34}$$

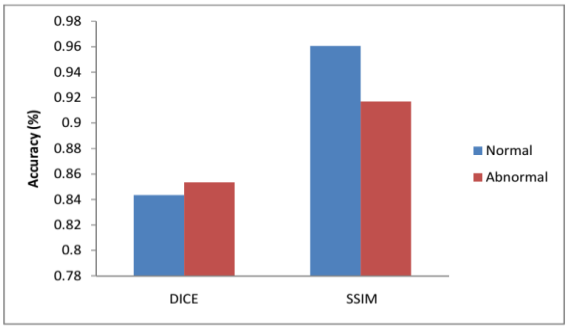

Figure 7: Segmentation accuracy performance

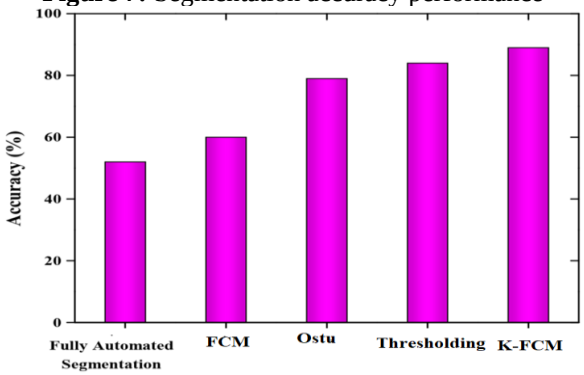

Figure 8: State-of-the-art segmentation accuracy r

Figure 8 shows the current segmentation results. We look at the precision of the proposed K-division FCM with that of existing division approaches, for example, a completely programmed division model, limit, FCM, and Otsu. When segmenting small invariant clusters, Thresholding strategies like Otsu function admirably, yet not as well as completely robotized division models like FCM, Limit, and K-FCM. Bunching approaches like FCM, Thresholding, and K-FCM achieve segmentation accuracy of 79 percent, 84 percent, and 89 percent, respectively. Compared with other current techniques such as Otsu, fully automatic segmentation model, FCM, and thresholding, the proposed K-FCM method achieved better segmentation results.

Figure 9 shows a comparison of the overall execution time graphs. AI (ML) [10], AI and picture handling (ML-IP) [12], dynamic diagram cutting with innocent Bayes (GC-NB) [13], and profound learning (DL) [14], technique has been distinguished. Complete time is determined in a flash. Results show that the proposed approach requires some investment to run than different calculations like ML, ML-IP, GC-NB, and DL

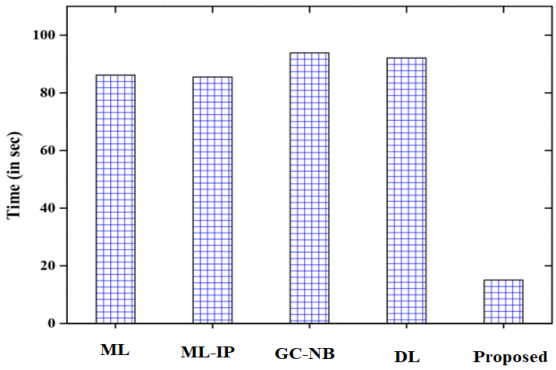

Figure 9: Segmentation accuracy results

The disarray framework's is displayed in Figure .10.The expected and actual categories of skin disease categorization accuracy based on normal and abnormal are described.

Actual Category		Predicted Category	
		Normal	Abnormal
	Normal	95%	5%
	Abnormal	8%	92%

Figure 10: Segmentation accuracy results

Figure 11 shows the results of the comparative study on the overall performance of skin infection testing. The te chnology verifies the effectiveness of dermatology diagnosis using ML, ML-IP, GC-NB, DL with parameters such as MCC, specificity, sensitivity, accuracy and F-score. The results showed that the method had an MCC of 99.27%, specificity of 99.32%, sensitivity of 99.02%, accuracy of 99.34%, and an F-score of 99.27%. The plan proposed an alternative to the current system in terms of division of labour**.**

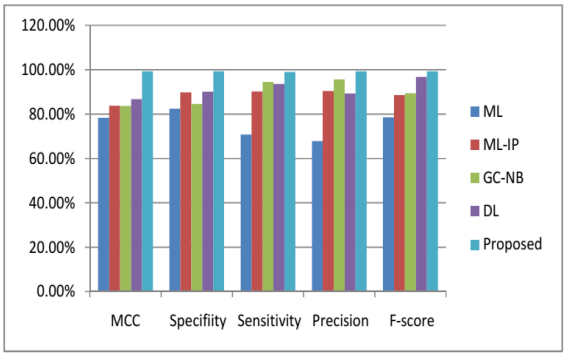

Figure 11: Overall performance kin disease classification

5.Conclusion:

For the skin disease categorization, A deep long short-term memory (CNN-LSTM) architecture with (TSA) is presented in this article The dataset picture details are picked from the Herlev dataset in Denmark, and the MATLAB software was used as the execution framework. We used 70% of the entire number of images for training and 30% for testing out of the entire amount of photos. The original image is turned into various angles to evaluate the enhancement effectiveness. When employing K-FCM algorithms, a higher SSIM and DICE

number suggests better segmentation outcomes. The suggested K-FCM approach outperformed the existing FCM, fully automated segmentation model, otsu, and thresholding methods in terms of segmentation accuracy, with an 89 % success rate. Using the suggested DLSTM-TSA superior prediction accuracy values are produced which are lower than those found using other current techniques such as ML, DL, GC-NB, and ML-IP.

Compliance with ethical standards

Conflict of interest

The authors declare that they have no conflict of interest.

Human and Animal Rights

No human or animal research has been conducted by any author.

Informed Consent

Consent was denied because this was a retrospective review without de-identified patient data.

Funding: Not included

Disclaimer: No

Permission to contribute: No

Permission to reprint: No

Yes data and information:

The data shared is not relevant to this article because no This New data was created or analyzed in the research.

Code Availability: None

References:

[1] Kolkur, S. and Kalbande, D.R., 2016, November. Survey of texture based feature extraction for skin disease detection. In 2016 International Conference on ICT in Business Industry & Government (ICTBIG) (pp. 1-6). IEEE.

[2] Dubal, P., Bhatt, S., Joglekar, C. and Patil, S., 2017, November. Skin cancer detection and classification. In 2017 6th international conference on electrical engineering and informatics (ICEEI) (pp. 1-6). IEEE.

[3] Kolkur, S., Kalbande, D.R. and Kharkar, V., 2018. Machine learning approaches to multi-class human skin disease detection. International Journal of Computational Intelligence Research, 14(1), pp.1-12.

[4] Velasco, J., Pascion, C., Alberio, J.W., Apuang, J., Cruz, J.S., Gomez, M.A., Molina Jr, B., Tuala, L., Thio-ac, A. and Jorda Jr, R., 2019. A smartphone-based skin disease classification using mobilenetcnn. arXiv preprint arXiv:1911.07929.

[5] Okuboyejo, D.A., Olugbara, O.O. and Odunaike, S.A., 2013, October. Automating skin disease diagnosis using image classification. In proceedings of the world congress on engineering and computer science (Vol. 2, pp. 850-854).

[6] Ubale, A.V. and Paikrao, P.L., 2019. Detection and Classification of Skin Diseases using Different Color Phase Models. no. July, pp.1331-1335.

[7] Okuboyejo, D.A., Olugbara, O.O. and Odunaike, S.A., 2013, October. Automating skin disease diagnosis using image classification. In proceedings of the world congress on engineering and computer science (Vol. 2, pp. 850-854).

[8] Kumar, M. and Kumar, R., 2016. An Intelligent System to diagnosis the skin disease. ARPN JEAS, 11(19), pp.11368-11373.

[9] Ubale, A.V. and Paikrao, P.L., 2019. Detection and Classification of Skin Diseases using Different Color Phase Models. no. July, pp.1331-1335.

[10] Bhadula, S., Sharma, S., Juyal, P. and Kulshrestha, C., 2019. Machine learning algorithms based skin disease detection. International Journal of Innovative Technology and Exploring Engineering (IJITEE), 9(2).

[11] Chakraborty, S., Mali, K., Chatterjee, S., Anand, S., Basu, A., Banerjee, S., Das, M. and Bhattacharya, A., 2017, October. Image based skin disease detection using hybrid neural network coupled bag-of-features. In 2017 IEEE 8th Annual Ubiquitous Computing, Electronics and Mobile Communication Conference (UEMCON) (pp. 242-246). IEEE.

[12] ALEnezi, N.S.A., 2019. A method of skin disease detection using image processing and machine learning. Procedia Computer Science, 163, pp.85-92.

[13] Balaji, V.R., Suganthi, S.T., Rajadevi, R., Kumar, V.K., Balaji, B.S. and Pandiyan, S., 2020. Skin disease detection and segmentation using dynamic graph cut algorithm and classification through Naive Bayes classifier. Measurement, 163, p.107922.

[14] Khamparia, A., Singh, P.K., Rani, P., Samanta, D., Khanna, A. and Bhushan, B., 2021. An internet of health things-driven deep learning framework for detection and classification of skin cancer using transfer learning. Transactions on Emerging Telecommunications Technologies, 32(7), p.e3963.

[15] Yu, L., Chen, H., Dou, Q., Qin, J. and Heng, P.A., 2016. Automated melanoma recognition in dermoscopy images via very deep residual networks. IEEE transactions on medical imaging, 36(4), pp.994-1004.

[16] Chen, Y., Li, J., Zhang, H., Zheng, Y., Jeon, B. and Wu, Q.J., 2016. Non-local-based spatially constrained hierarchical fuzzy C-means method for brain magnetic resonance imaging segmentation. IET Image Processing, 10(11), pp.865-876.

[17] Memon, K.H. and Lee, D.H., 2018. Generalised kernel weighted fuzzy C-means clustering algorithm with local information. Fuzzy Sets and Systems, 340, pp.91-108.

[18] Wu, C. and Cao, Z., 2021. Noise distance driven fuzzy clustering based on adaptive weighted local information and entropy-like divergence kernel for robust image segmentation. Digital Signal Processing, 111, p.102963.

[19] Kolkur, S. and Kalbande, D.R., 2016, November. Survey of texture based feature extraction for skin disease detection. In 2016 International Conference on ICT in Business Industry & Government (ICTBIG) (pp. 1-6). IEEE.

[20] Chatterjee, S., Dey, D. and Munshi, S., 2019. Integration of morphological preprocessing and fractal based feature extraction with recursive feature elimination for skin lesion types classification. Computer methods and programs in biomedicine, 178, pp.201-218.

[21] Wang, F., Xuan, Z., Zhen, Z., Li, K., Wang, T. and Shi, M., 2020. A day-ahead PV power forecasting method based on LSTM-RNN model and time correlation modification under partial daily pattern prediction framework. Energy Conversion and Management, 212, p.112766.
[22] Messina, R. and Louradour, J., 2015, August. Segmentation-free handwritten Chinese text recognition with LSTM-RNN. In 2015 13th International conference on document analysis and recognition (icdar) (pp. 171-175). IEEE.
[23] Kaur, S., Awasthi, L.K., Sangal, A.L. and Dhiman, G., 2020. Tunicate Swarm Algorithm: A new bio-inspired based metaheuristic paradigm for global optimization. Engineering Applications of Artificial Intelligence, 90, p.103541.
[24] Houssein, E.H., Helmy, B.E.D., Elngar, A.A., Abdelminaam, D.S. and Shaban, H., 2021. An improved tunicate swarm algorithm for global optimization and image segmentation. IEEE Access, 9, pp.56066-56092.
[25] Yang, M., Tu, W., Wang, J., Xu, F. and Chen, X., 2017, February. Attention based LSTM for target dependent sentiment classification. In Proceedings of the AAAI Conference on Artificial Intelligence (Vol. 31, No. 1).
[26] Wu, D. and Chi, M., 2017. Long short-term memory with quadratic connections in recursive neural networks for representing compositional semantics. IEEE Access, 5, pp.16077-16083.
[27] Essaid, M., Kim, D., Maeng, S.H., Park, S. and Ju, H.T., 2019, September. A collaborative DDoS mitigation solution based on ethereum smart contract and RNN-LSTM. In 2019 20th Asia-Pacific Network Operations and Management Symposium (APNOMS) (pp. 1-6). IEEE.
[28] Agafonov, A.A. and Yumaganov, A.S., 2019. Bus arrival time prediction using recurrent neural network with LSTM architecture. Optical Memory and Neural Networks, 28(3), pp.222-230.
[29] Roy, S.K., Manna, S., Dubey, S.R. and Chaudhuri, B.B., 2019. LiSHT: Non-parametric linearly scaled hyperbolic tangent activation function for neural networks. arXiv preprint arXiv:1901.05894.
[30] Jerant, A.F., Johnson, J.T., Sheridan, C.D. and Caffrey, T.J., 2000. Early detection and treatment of skin cancer. American family physician, 62(2), pp.357-368.
[31] Jain, S. and Pise, N., 2015. Computer aided melanoma skin cancer detection using image processing. Procedia Computer Science, 48, pp.735-740.
[32] Sigurdsson, S., Philipsen, P.A., Hansen, L.K., Larsen, J., Gniadecka, M. and Wulf, H.C., 2004. Detection of skin cancer by classification of Raman spectra. IEEE transactions on biomedical engineering, 51(10), pp.1784-1793.
[33] Milton, M.A.A., 2019. Automated skin lesion classification using ensemble of deep neural networks in ISIC 2018: Skin lesion analysis towards melanoma detection challenge. arXiv preprint arXiv:1901.10802.
[34] Kinyanjui, N.M., Odonga, T., Cintas, C., Codella, N.C., Panda, R., Sattigeri, P. and Varshney, K.R., 2019. Estimating skin tone and effects on classification performance in dermatology datasets. arXiv preprint arXiv:1910.13268.
[35] Koh, H.K., Geller, A.C., Miller, D.R., Grossbart, T.A. and Lew, R.A., 1996. Prevention and early detection strategies for melanoma and skin cancer: current status. Archives of dermatology, 132(4), pp.436-443.
[36] Chaudhari, R., Vora, J.J., Mani Prabu, S.S., Palani, I.A., Patel, V.K., Parikh, D.M. and de Lacalle, L.N.L., 2019. Multi-response optimization of WEDM process parameters for machining of superelastic nitinol shape-memory alloy using a heat-transfer search algorithm. Materials, 12(8), p.1277.
[37] Chaudhari, R., Vora, J.J., Patel, V., López de Lacalle, L.N. and Parikh, D.M., 2020. Surface analysis of wire-electrical-discharge-machining-processed shape-memory alloys. Materials, 13(3), p.530.